AGU PUBLICATIONS

JGR

Journal of Geophysical Research: Oceans

RESEARCH ARTICLE

10.1002/2014JC010173

Quad-polarization SAR features of ocean currents

V. Kudryavtsev[1,2,3], I. Kozlov[1], B. Chapron[1,4], and J. A. Johannessen[3]

[1]Satellite Oceanography Laboratory, Russian State Hydrometeorological University, St. Petersburg, Russia, [2]Department of Remote Sensing, Marine Hydrophysical Institute, Sebastopol, Russia, [3]Nansen Environmental and Remote Sensing Center, Bergen, Norway, [4]Laboratoire d'Oceanographie Spatiale, Ifremer, Plouzane, France

Key Points:
- A methodology to exploit polarization sensitivity to interpret SAR images
- Current signatures are mostly dominated by nonpolarized breaking scatters
- Analysis clearly demonstrates impact of breakers on cross-polarized signals

Correspondence to:
V. Kudryavtsev,
kudr@rshu.ru

Citation:
Kudryavtsev, V., I. Kozlov, B. Chapron, and J. A. Johannessen (2014), Quad-polarization SAR features of ocean currents, *J. Geophys. Res. Oceans*, *119*, 6046–6065, doi:10.1002/2014JC010173.

Received 21 MAY 2014
Accepted 17 AUG 2014
Accepted article online 21 AUG 2014
Published online 15 SEP 2014

Abstract A methodology is demonstrated to exploit the polarization sensitivity of high-resolution radar measurements to interpret and quantify upper ocean dynamics. This study particularly illustrates the potential of quad-polarization synthetic aperture radar (SAR) measurements. The analysis relies on essential characteristics of the electromagnetic scattering mechanisms and hydrodynamical principles. As the relaxation scale of centimeter-scale ocean surface scatters is typically small, radar signal anomalies associated with surface manifestations of the upper ocean dynamics on spatial scales exceeding 100 m are mostly dominated by nonresonant and nonpolarized scatters. These "scalar" contributions can thus efficiently trace local breaking and near-breaking areas, caused by surface current variations. Using dual copolarized measurements, the polarized Bragg-type radar scattering is isolated by considering the difference (PD) between vertically and horizontally polarized radar signals. The nonpolarized (NP) contribution associated with wave breaking is then deduced, using the measured polarization ratio (PR) between polarized signals. Considering SAR scenes depicting various surface manifestations of the upper ocean dynamics (internal waves, mesoscale surface current features, and SST front), the proposed methodology and set of decompositions (PD, PR, and NP) efficiently enable the discrimination between surface manifestation of upper ocean dynamics and wind field variability. Applied to quad-polarized SAR images, such decompositions further provide unique opportunities to more directly assess the cross-polarized (CP for HV or VH) signal sensitivity to surface roughness changes. As demonstrated, such an analysis unambiguously demonstrates and quantitatively evaluates the relative impact of breakers on cross-polarized signals under low to moderate wind conditions.

1. Introduction

Spectacular manifestations of mesoscale and submesoscale ocean surface signatures are often reported using active and passive high-resolution satellite sensors, i.e., from active microwave synthetic aperture radars (SARs) and optical radiometers viewing areas in and around the sun glitter [e.g., *Kudryavtsev et al*., 2012a, 2012b]. Mostly under "favorable" low to moderate wind speeds, these images trace local ocean surface "roughness" anomalies resulting from interactions of wind waves with nonuniform surface currents, transformation of the near-surface wind field over large SST gradients, and/or suppression of short waves in surface slicks accumulated by surface current convergences [e.g., *Marmorino et al*., 1994; *Jansen et al*., 1998; *Johannessen et al*., 2005; *McWilliams et al*., 2009; *Kudryavtsev et al*., 2012b; *Rascle et al*., 2014]. Among these various oceanic phenomena, internal waves (IWs) are often reported [e.g., *Jackson*, 2007; *Liu et al*., 2014] but also serve as test beds to assess forward imaging model to advance the quantitative interpretation of high-resolution satellite observations [*Alpers and Hennings*, 1984; *Thompson*, 1988; *Lyzenga and Bennett*, 1988; *Romeiser and Alpers*, 1997; *Kudryavtsev et al*., 2005].

Compared to optical observations, all-weather radar images can further help to quantitatively separate the measured roughness variations between changes associated with denser breaking patches and purely resonant short-scale scatter modulations. This capability relates to the polarization sensitivity of radar signals. Polarization sensitivity, such as the difference between vertically (VV) and horizontally (HH) polarized radar signals, is indeed characteristic of a resonant scattering mechanism mostly governed by small surface scales. Such a property must then help to efficiently trace centimeter-scale wave variations [e.g., *Mouche et al*., 2007a, 2007b; *Guerin et al*., 2010]. As recently demonstrated using dual copolarized SAR measurements [*Kudryavtsev et al*., 2013], this enables a very effective methodology to interpret and quantitatively assess different detected surface ocean phenomena.

Moreover, the relaxation scale of the short resonant-Bragg waves is rather small, from 10 to 100 m [*Phillips*, 1984; *Kudryavtsev et al*., 2005]. Accordingly, currents with spatial scales of variation exceeding 100 m cannot explain the measured surface manifestations. Intermediate-scale steeper wave breaking or near-breaking effect on microwave scattering must then be considered [*Lyzenga*, 1996; *Chubb et al*., 1999; *Jansen et al*., 1998]. More generally, enhanced roughness patches may give both enhanced Bragg and scalar scattering that possibly dominate the radar returns. This approach had been developed [*Kudryavtsev et al*., 2005] with a physically based radar imaging model (RIM), where this impact was incorporated via the energy balance of short waves, and the introduction of an extra energy source due to mechanical disturbances of the surface by larger-scale breakers. Such a development led to significant improvement to reproduce SAR signatures for a variety of the ocean phenomena.

Local signatures of breaking patches can be isolated by using HH and VV-polarized radar signals [*Kudryavtsev et al*., 2013]. A decomposition of the normalized radar cross section of the ocean surface is suggested as a sum of polarized scattering, associating with two-scale resonant Bragg-scattering (σ_{0B}^{pp}), and nonpolarized scattering (σ_{wb}) mostly dominated by breaking patches [e.g., *Chapron et al*., 1997; *Quilfen et al*., 1999]:

$$\sigma_0^{pp} = \sigma_{0B}^{pp} + \sigma_{wb}. \tag{1}$$

From copolarized, VV and HH measurements, the wave breaking contribution is removed using the polarization difference (PD):

$$\Delta\sigma_0 \equiv \sigma_0^{vv} - \sigma_0^{hh} = \sigma_{0B}^{vv} - \sigma_{0B}^{hh}. \tag{2}$$

The polarization difference is largely controlled by centimeter-resonant Bragg waves. Because of their "quick-response" to wind forcing (relaxation scale of order of 10 m), the PD must closely reflect the near-surface wind variability and eventual presence of surface slicks.

The redistribution of radar returns between short-scale Bragg waves and wave breaking is then characterized by the polarization ratio (PR):

$$P = \frac{\sigma_{0B}^{hh} + \sigma_{wb}}{\sigma_{0B}^{vv} + \sigma_{wb}}. \tag{3}$$

This ratio is minimal for the pure Bragg scattering and approaches $P=1$ when σ_{wb} dominates. In fact, reported PR measurements systematically deviate from the Bragg model predictions [see, e.g., *Mouche et al*., 2006, and references therein]. As generally found for Ku and C-band measurements, $P=\sigma_0^{hh}/\sigma_0^{vv}$ always exceeds the polarization ratio following from the two-scale resonant Bragg scattering model, $p_B=\sigma_{0B}^{hh}/\sigma_{0B}^{vv}$. Observed PR also has larger azimuth variations [*Mouche et al*., 2007a]. From (1) and (2), the nonpolarized (NP) radar backscatter component, σ_{wb}, can be evaluated as

$$\sigma_{wb} = \sigma_0^{vv} - \Delta\sigma_0/(1-p_B). \tag{4}$$

Based on (1)–(4), the original copolarized VV and HH images may be decomposed into PD, PR, and NP images. This decomposition discriminates between fast-responding Bragg waves and wave breaking patches, thus providing an effective tool for separating the ocean surface currents features [*Kudryavtsev et al*., 2013].

Moreover, applied to quad-polarized SAR images, such decomposition provides a unique opportunity to assess the cross-polarized (CP; HV or/and VH) signal sensitivity to the surface roughness, and more specifically its sensitivity to wave breaking. Indeed, the ratio, CP/PD, will be further used to assess efficiency of the Bragg scattering mechanism to explain observed radar backscatter features at cross-polarization. Recent analyses [*Hwang et al*., 2010; *Voronovich and Zavorotny*, 2011; *Zhang et al*., 2011] have demonstrated significant excess of observed CP signal over the models (either two-scale Bragg model and small-slope approximation of the second order model (SSA2)), and its enhanced wind sensitivity at high wind conditions that was largely attributed to the impact of wave breaking.

The proposed radar signal decomposition is especially valuable for investigation of the upper ocean dynamics as already demonstrated in *Kudryavtsev et al*. [2013]. Capitalizing on that approach, this paper aims to provide further insight on the physics of the radar imaging of spatially varying ocean surface currents. For this purpose, observations of internal waves and sea surface frontal features in the White Sea are selected

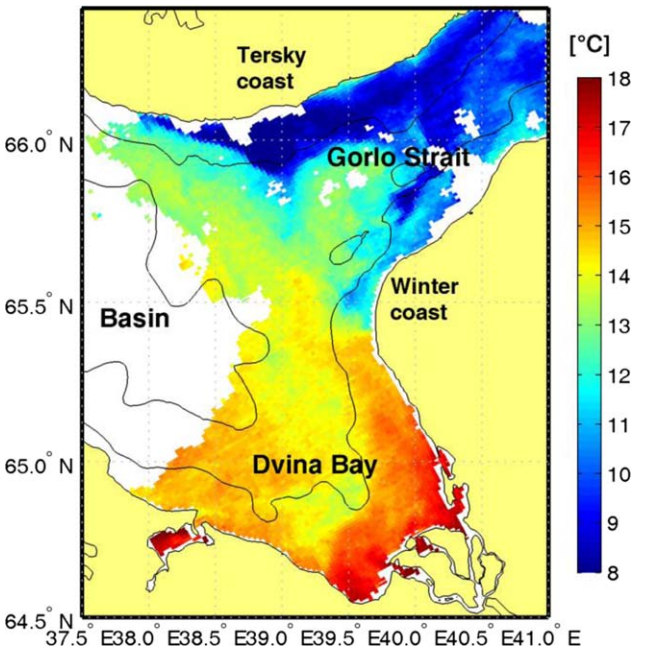

Figure 1. Map of the eastern White Sea with MODIS Aqua SST (28 July 2012 at 09:05 UTC) and overlain bathymetry contours at 50 m intervals. Bathymetry map is obtained from IBCAO Grid version 3.0 [*Jakobsson et al.*, 2012].

as a test bed to demonstrate the potential of the proposed radar image analysis. We have quantitatively evaluated and unambiguously demonstrated that wave breaking play the dominant role in the formation of dual copolarized and cross-polarized SAR signatures of the upper ocean dynamics.

This paper is organized as following. The data and study area is presented in section 2 followed by a discussion of the radar imaging properties in section 3. In section 4 the quad-polarized method is then applied to the analyses of distinct current features followed by a corresponding discussion in section 5. The conclusion then follows in section 6.

2. Data and Study Area

This study is based on quad-polarized RADARSAT-2 SAR images acquired in the southwestern part of the Gorlo Strait which connects the White Sea and the Barents Sea (Figure 1) on 29 July 2012 (14:45 UTC) and 1 August 2012 (14:58 UTC). Overall nine frames of RADARSAT-2 SAR images in the Wide Fine Quad-Pol beam mode (Single Look Complex product) were acquired. Each of the SAR frames covers about 40 × 50 km on the surface at nominal resolution of 5.2 and 7.6 m in range and azimuth direction, respectively (Figure 2).

The Gorlo Strait is 50 km wide, 150 km long, and 40 m deep. It is well mixed in the vertical except during the spring river flood [*Glukhovsky*, 1991]. However, the southwestern part of the strait is subject to a complex interplay of different water masses transported by the outgoing (from the White Sea to the Barents Sea) fresh and warm current along the Winter Coast (Figure 1, southeastern coast) and the incoming saline and cold water along the Tersky Coast (northwestern coast) [*Shapiro et al.*, 2003]. As a result, a strong

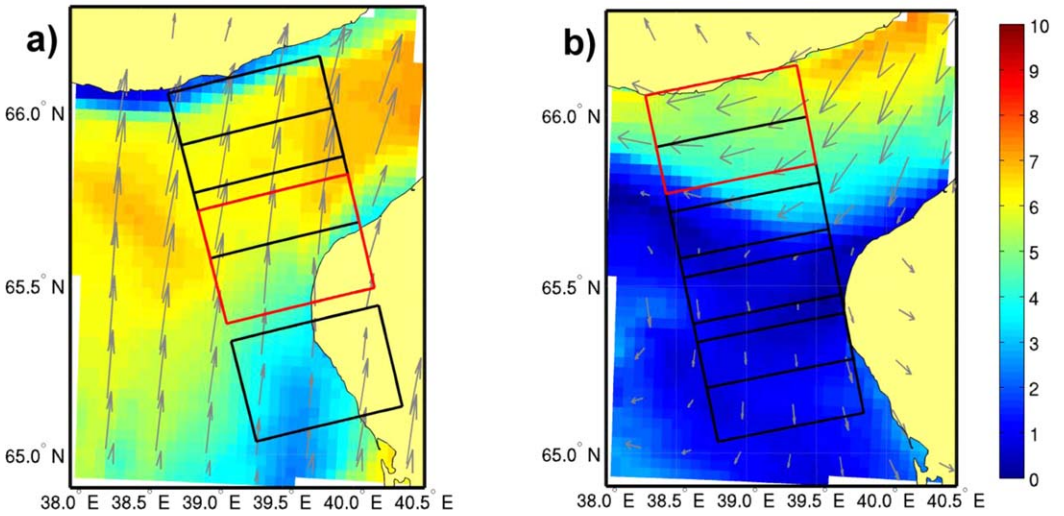

Figure 2. Wind velocity at 10 m height in the northwestern White Sea from MM5 model on (a) 29 July 2012 and (b) 1 August 2012 with RADARSAT-2 SAR frame swaths overlain. SAR frames marked by red are considered in the present study.

density front is usually present in the southwestern part of the Gorlo Strait. In addition, both the currents and frontal dynamics are strongly affected by intense tides and bottom topography [*Shapiro et al*., 2003; *Kozlov et al*., 2014].

Winds over the Gorlo Strait experience strong variability (Figure 2). During the first SAR image acquisition on 29 July 2012 (Figure 2a), southerly moderate winds dominate the area. In contrast, the second SAR image (1 August 2012) is taken at northerly winds that sharply change across an atmospheric front located over the southern part of the Gorlo Strait (Figure 2b). For further analysis we use the SAR-derived wind speed (using CMOD4 geophysical model function of *Stoffelen and Anderson* [1997]) and MM5-simulated wind direction.

The original SAR data were first calibrated in NRCS units and then the thermal noise correction was applied [*MacDonald*, *Dettwiler and Associates Ltd*., 2013]. Finally, the SAR images were smoothed using the adaptive Wiener filter with the moving 20-by-20 pixels window. This study focuses on two particular SAR scenes shown in Figures 3 and 4. These SAR scenes exhibit a variety of SAR signatures of the upper ocean dynamics including internal waves and mesoscale current features. They also manifest "natural" wind variability, wind changes caused by wind transformation over the SST front located in the southwestern Gorlo Strait (Figure 1), as well as the surface roughness signatures of the atmospheric internal waves (Figure 4).

Both the VV and HH SAR frames (Figure 3) exhibit distinct bright/dark linear features near the Winter Coast, which trace the alongshore stream from the Dvina Bay. Another remarkable features are the elongated bright/dark radial signatures associated with trains of internal waves. A large-scale change of the wind field is also well detected in these frames.

In the SAR scene shown in Figure 4, the main feature is a dark area adjacent to the coast. It coincides with a near-coastal cold SST area (Figure 1). The dark area in the HH image is bounded by a thin "bright" line, which, however, is not visible in the VV image. Periodic bright/dark wave-like patterns, presumably caused by near-surface wind variations induced by atmospheric internal gravity waves, are also noticeable.

3. Background Properties of the NRCS

The mean radar scattering properties (PR, PD, and NP) derived from the two RADARSAT-2 SAR correspond well to similar properties derived by *Mouche et al*. [2012] from the global ENVISAT data (Figure 5). The best correspondence with ENVISAT is found for the polarization ratio (Figure 5a). Observed PR depends weakly on wind speed and apparently exceeds the two-scale Bragg-scattering model predictions.

The polarization difference is strongly wind-dependent. Its wind exponent varies around 1.5–2 in either cross-wind or up-wind radar look directions (Figure 5b). At moderate winds and the up-wind radar look

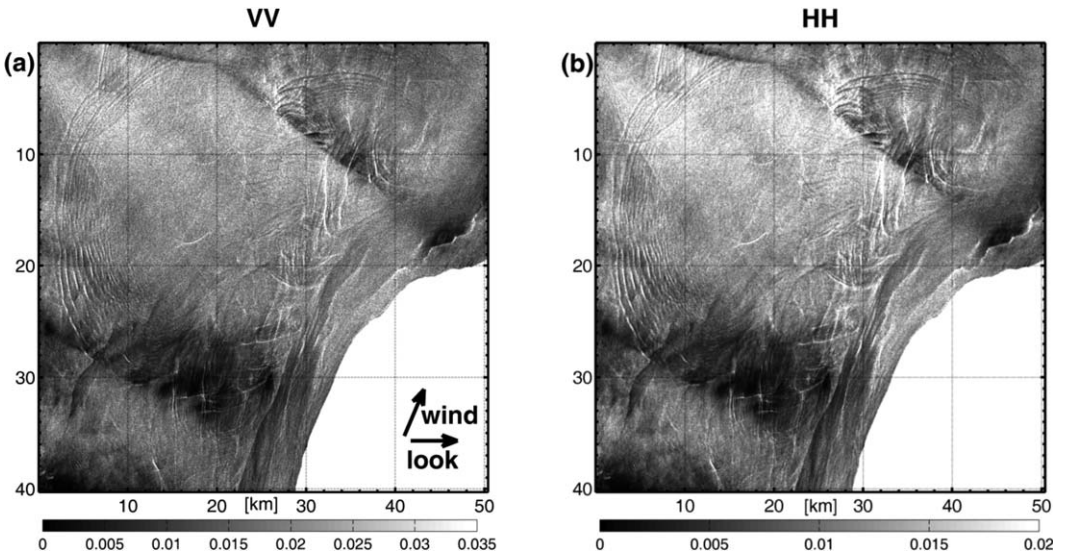

Figure 3. RADARSAT-2 SAR (a) VV and (b) HH images (in linear units) acquired on 29 July 2012 at 14:45 UTC (frame RS2_FQA_1xQGSS20120729_144551_00000005xQ12_704 16bxx_24139_FC556) with manifestations of alongshore current and trains of internal waves. The incidence angle ranges from 30.6° to 33.6°. The arrows indicate the model wind and radar look directions. © MDA © CSA.

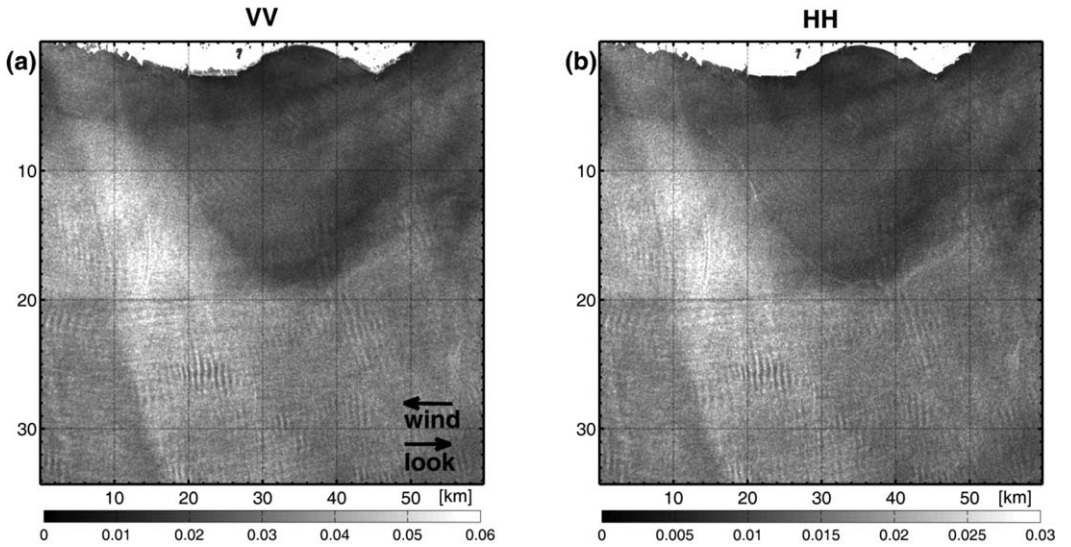

Figure 4. RADARSAT-2 SAR (a) VV and (b) HH NRCS (in linear units) over the northeastern White Sea acquired on 1 August 2012 at 14:58 UTC (frame RS2_FQA_1xQGSS20120801_145829_00000004xQ19_16bxx_24182_FE6F8) depicting manifestations of the SST front. The incidence angle ranges from 37.7° to 40.4°. The arrows indicate the model wind and radar look directions. © MDA © CSA.

direction, our local (the White Sea) PD observations are very close to PD derived from the global ENVISAT observations. At lower winds and the cross-wind direction, the differences from the global data are noticeable (Figure 5b). This is not surprising as the global data at low cross-winds include wider variety of conditions including wind gustiness and variability in the sea state (including SST that impacts the wave dissipation). This variety of conditions may affect the local and global statistics at low cross-winds.

The NP contribution to the SAR NRCS (4) reflects the wave breaking contribution (σ_{wb}) and strongly depends on wind speed (Figure 5c). Its wind exponent varies depending on wind speed and direction. At low winds (cross-wind direction, incidence angle $\theta = 32°$) the wind exponent is about 2.5. While at moderate winds (up-wind direction, $\theta = 38.5°$) the wind exponent is about 1.5. The local NP values are consistent with the global estimates except at very low winds below 5 m/s. Both up-wind and cross-wind data are available at wind speed of about 5 m/s where the cross-wind NP overshoots the up-wind NP (Figure 5c), which is explained by lower incidence angle for the cross-wind data as well as azimuth dependency of NP. At low winds and the cross-wind radar look directions, NP $\sim$ PD^2 (Figure 5d) indicating that wave breaking grows faster with wind speed as the Bragg waves do. At moderate winds and the up-wind radar look, NP and PD are almost linear-dependent. The difference from the global "NP-vs-PD" relationship results from the associated difference in PD at low winds (Figure 5b) discussed above.

Note that NP (equation (4)) depends on the two-scale Bragg polarization ratio, p_B, and on uncertainties of its definition. Bragg polarization ratio mainly depends on the incidence angle, does not depend on Bragg waves spectrum, and weakly depends on the mean square slope (MSS) of tilting waves in direction of the incidence plane. MSS of tilting waves can be prescribed by empirical relation (e.g., by the relation suggested by *Phillips* [1977] for the slick surface, which was used to calculate p_B shown in Figure 5) or calculated from a spectrum model (see, e.g., examples of MSS and p_B calculations for different spectra in *Hwang and Plant* [2010]). Apparently, an uncertainty in definition of the MSS (and thus in p_B) leads to an "error" of NP calculations, which can be assessed as:

$$\frac{\delta\sigma_{wb}}{\sigma_{wb}} = -\frac{\Delta\sigma_0}{\sigma_{wb}}\frac{\delta p_B}{(1-p_B)^2}, \tag{5}$$

where $\delta\sigma_{wb}$ is NP "error" caused by uncertainties in definition of Bragg polarization ratio δp_B. For the data shown in Figure 5, variation $\delta p_B/p_B = \pm 0.1$ results in $\delta\sigma_{wb}/\sigma_{wb} \approx \mp 0.2$ "error" in NP calculation.

Wind speed dependencies of the local cross-polarized NRCS, CP$=(\sigma_0^{vh}+\sigma_0^{hv})/2$, are shown in Figure 6 for 1 August 2012 data (for the 29 July 2012 image, the winds are too low, and CP NRCS is on the noise-floor are therefore not shown). The CP signal appears strongly wind-dependent, with wind exponent of about 1.5. The

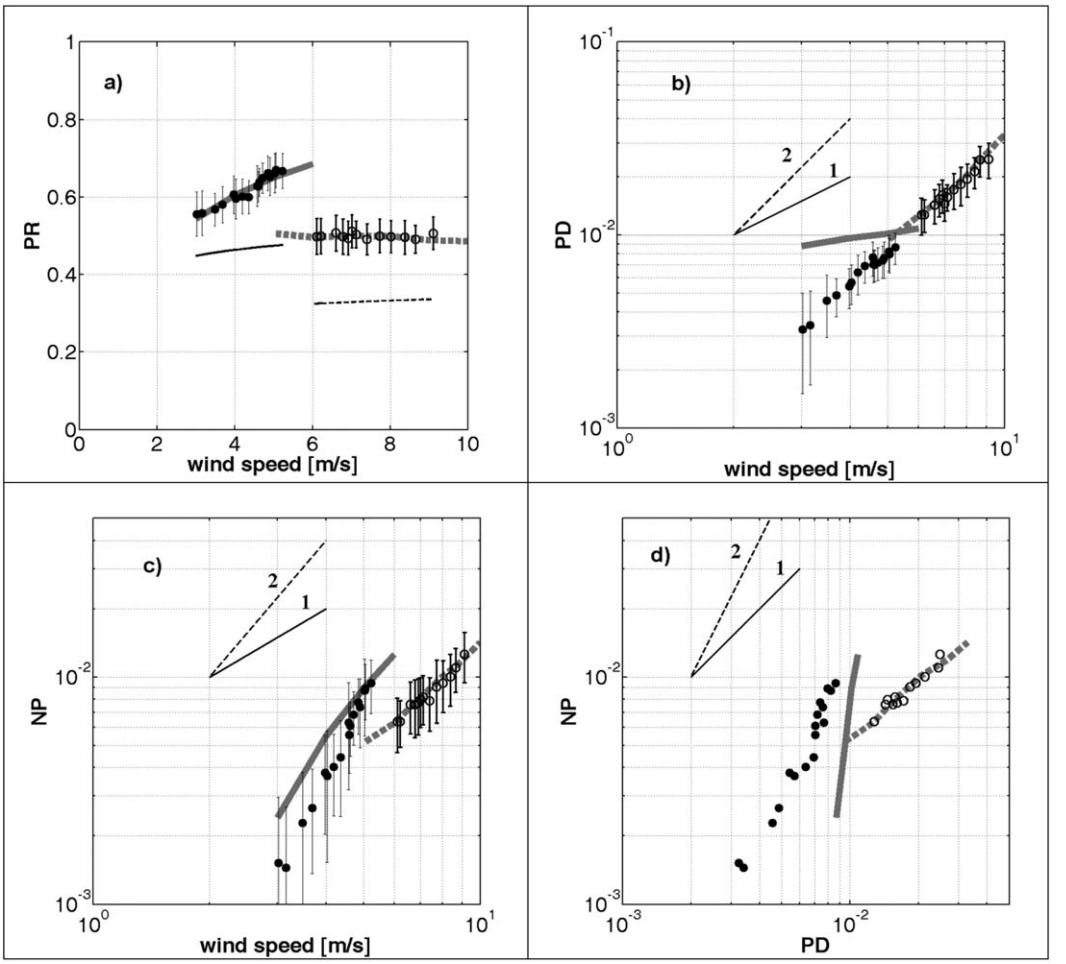

Figure 5. Background properties of the NRCS derived from RADARSAT-2 SAR images on 29 July 2012 and 1 August 2012: (a) polarization ratio, PR (HH/VV), versus SAR wind speed; (b) polarization difference, PD (VV-HH), versus SAR wind speed; (c) nonpolarized part of the NRCS, NP, versus SAR wind speed; (d) NP versus PD. All quantities are given in linear units. Filled circles are from the SAR data on 29 July 2012 (cross-wind direction at incidence angle 32° ± 0.25°); open circles are from the SAR data on 1 August 2012 (up-wind direction at incidence angle 38.5° ± 0.25°). Vertical bars indicate the standard deviation of the SAR observations. Black solid and dash lines in Figure 5a show two-scale Bragg model prediction for the SAR observations in cross-wind and up-wind directions, correspondingly. Thick gray lines show the *Mouche et al.* [2012] relationships built on empirical dual-pol globally averaged ENVISAT radar data for the cross-wind direction (gray solid) and up-wind direction (gray dash). Lines marked by "1" and "2" indicate corresponding power laws.

ratio CP over PD, CP/PD, can be used to assess the ability of the two-scale Bragg scattering mechanism to describe cross-polarized radar backscattering. Following the two-scale Bragg model [*Valenzuela*, 1978], CP reads:

$$\sigma_{0B}^{vh} = \pi \sin^{-4}\theta |G_{vv} - G_{hh}|^2 \frac{s_n^2}{\sin^2\theta} B(\boldsymbol{k}_{br}), \tag{6}$$

where G_{pp} are known scattering coefficients, s_n^2 the mean square slope (MSS) of tilting waves out of the radar incidence plane, and $B(\boldsymbol{k}_{br})$ is the saturation spectrum at Bragg wavenumber. Using $\sigma_{0B}^{pp} = \pi \sin^{-4}\theta |G_{pp}|^2 B(\boldsymbol{k}_{br})$ for the copolarized pure Bragg NRCS, we get the following relationship for the two-scale Bragg model ratio $\sigma_0^{vh}/\Delta\sigma_0$, which is valid to the first order in MSS:

$$\frac{\sigma_0^{vh}}{\Delta\sigma_0} = \frac{|G_{vv} - G_{hh}|^2}{|G_{vv}|^2 - |G_{hh}|^2} \frac{s_n^2}{\sin^2\theta}, \tag{7}$$

and which is independent on the Bragg wave spectrum. In order to evaluate (7) we assume that slopes of the large-scale surface are isotropic; therefore, s_n^2 is half of the total large-scale surface MSS, $s_n^2 = 1/2 s^2$, prescribed by empirical relation [*Phillips*, 1977; *Vandemark et al.*, 2004]: $s^2 = 4.6 \times 10^{-3} \ln(k_d U_{10}^2/g)$, $k_d = k_{br}/4$ is dividing wavenumber for the tilting wave in the two-scale Bragg model, U_{10} is wind speed at 10 m height.

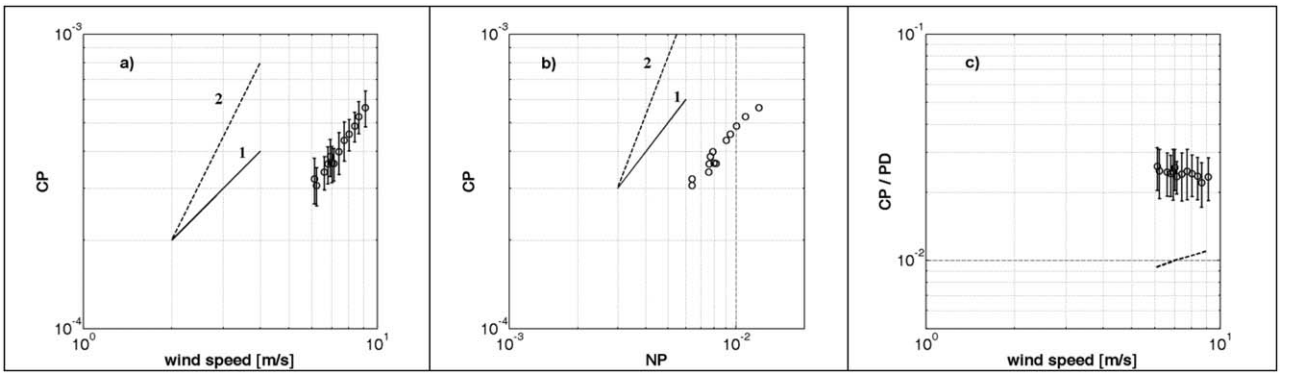

Figure 6. Background properties of the cross-pol NRCS, CP = (VH+HV)/2, derived from RADARSAT-2 SAR images on 1 August 2012: (a) CP versus SAR wind speed, (b) CP versus NP, (c) CP over PD ratio versus SAR wind speed. All quantities are given in linear units. Open circles are data derived from SAR image at up-wind direction, incidence angle 38.5° ± 0.25°. Black-dashed line in Figure 6c is the prediction of two-scale Bragg model at up-wind direction, incidence angle 38.5°. Vertical bars indicate standard deviation of SAR data. Lines marked by "1" and "2" indicate corresponding power laws.

The observed values of CP/PD (Figure 6) exceed (by factor 2.5, or about 4 dB) the two-scale Bragg model predictions (7). This difference may be interpreted as significant impact of nonlinear roughness elements associated with wave breaking on cross-polarized radar return even at moderate winds. However it should be noticed that classical two-scale Bragg model underestimates cross-polarized radar return as compared with more elaborate scattering models (e.g., small-slope approximation of the second order (SSA2) *Voronovich and Zavorotny* [2011, 2014]) due to ignoring the Bragg scattering of the second order. *Voronovich and Zavorotny* [2011, Figure 2] showed that the difference between CP NRCS calculated using SSA2 and two-scale Bragg model may attain 2 dB for winds above 15 m/s (at lower winds this difference is less 2 dB). Observed 4 dB departure of Bragg model ratio CP/PD from the data (Figure 6) exceeds 2 dB Bragg model deficit, and therefore it may be treated as a wave breaking impact. We also notice that significant departure of observed CP NRCS from either two-scale Bragg and SSA2 models at moderate and high winds has been reported by *Hwang et al*. [2010], *Voronovich and Zavorotny* [2011], and *Zhang et al*. [2011] and interpreted as impact of wave breaking.

4. Currents Manifestation

In this section, we apply the decomposition method to the internal waves (IW) and frontal features specifically manifested in the two RADARSAT-2 SAR images presented above.

4.1. Internal Waves

In Figure 7 the VV and HH images (displaced in Figure 3) are converted to the PR, PD, and NP images. The PD image contrasts (Figure 7c) are much weaker than the NP image contrasts (Figure 7d). Therefore, we can conclude that the modulation of the wave breaking by the surface currents dominates the SAR image contrasts over the modulation of the small-scale Bragg resonant waves. This conclusion is moreover supported by PR image (Figure 7b), which has larger PR values spatially correlated with the enhanced intensity of NP signals. This correlation indicates local redistribution of radar return between wave breaking and Bragg facets seen in larger PR corresponding to more intense wave breaking. Notice that due to the stronger wind dependence of wave breaking as compared to the Bragg waves (see Figure 5), the "large-scale" wind variability is also clearly expressed in the NP image.

The enlarged fragments (black box in Figure 7a) express a train of IWs in Figure 8, while a more "spaghetti-like" structure of IWs is depicted in Figure 9 together with a manifestation of the coastal current. In both cases, the radar expression of the surface signatures is much stronger in the NP images than in the PD images (this is more evident in Figure 9). The contrast profiles ($K_y = (y - \bar{y})/\bar{y}$, normalized deviation from the profile mean value) across the train of internal waves (marked as T1 in Figure 7a) demonstrate good IW detectability at both polarizations (Figure 10), but with larger HH amplitude. The strongest contrast is presented in the NP transect while PD contrast is apparently weaker. On average NP contrast of IW signatures is 7 times stronger than that for PD, $K_{NP} = 7 \times K_{PD}$ (Figure 11).

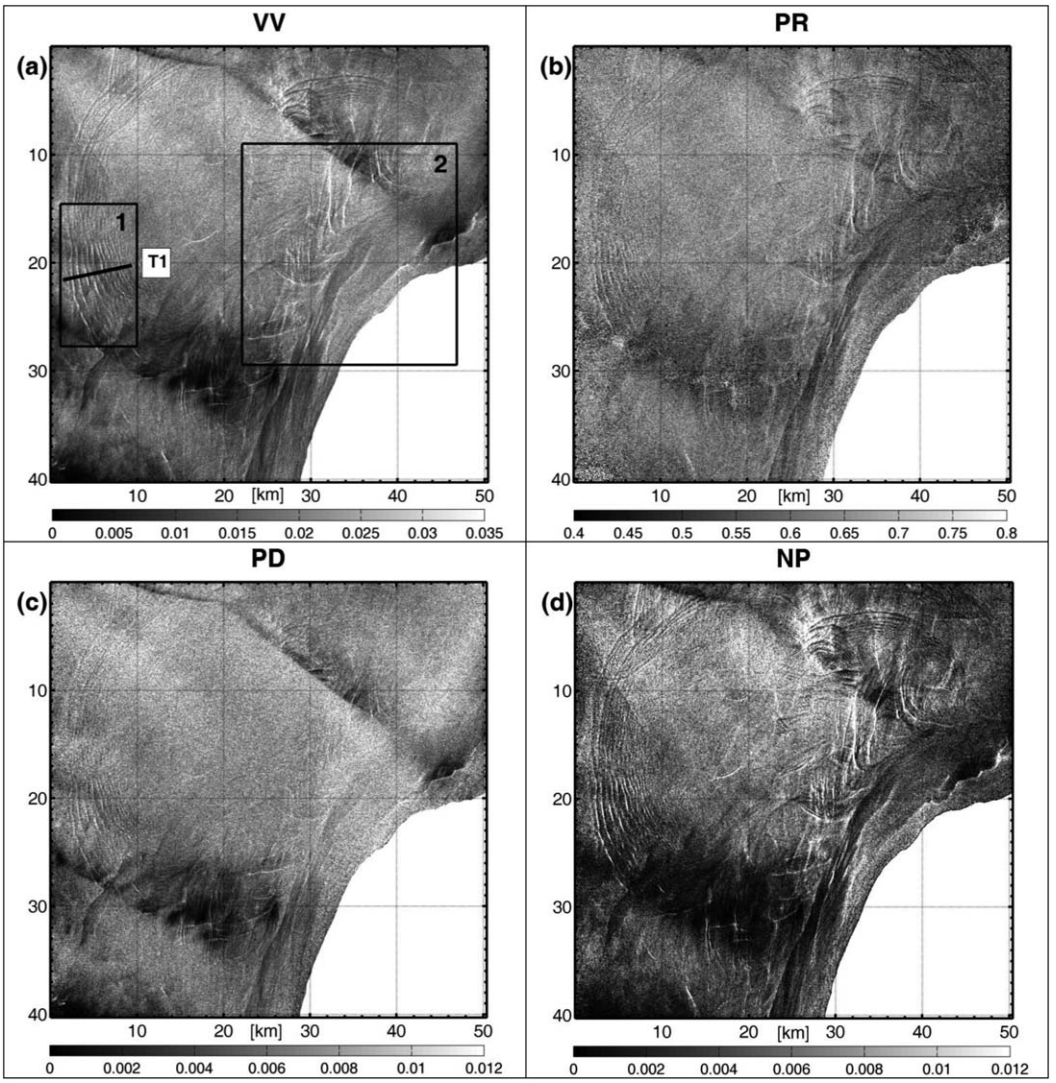

Figure 7. RADARSAT-2 SAR (a) original VV image shown in Figure 3, (b) polarization ratio, PR image, (c) polarization difference, PD image, and (d) nonpolarized contribution, NP image. Solid line in Figure 7a shows transect T1 across internal wave train. Black frames "1" and "2" indicate fragments shown in Figures 8 and 9. © MDA, © CSA.

The PD scenes in Figures 8 and 9 indicate that Bragg waves are apparently modulated by IWs. This is rather surprising noting fast Bragg wave response to wind forcing. The wave spectrum modulations depends on the ratio between the relaxation time, t_r, and the timescale of the wave-current interaction, T. If $t_r/T \ll 1$ the wave modulation vanishes, and the spectrum solely depends on the local wind. The relaxation time is estimated using the wind wave growth rate $\beta = c_\beta u_*^2/c^2$ and the wave spectrum wind exponent $m = \partial \ln B/\partial \ln u_*$ [see *Kudryavtsev et al.*, 2005, equation (39)]:

$$\omega t_r = (m c_\beta)^{-1} (c/u_*)^2, \tag{8}$$

where c_β is a growth rate "constant," u_* is the air friction velocity, ω and c are the wave frequency and phase speed. For IW $T \propto \Omega^{-1}$, therefore $t_r/T = (m c_\beta)^{-1}(\Omega/\omega)(c/u_*)^2$. At $u_* = 0.13$ m/s (observed wind speed of 4 m/s), IW frequency $\Omega = CK = 0.06$ rad/s (estimated via typical C = 0.5 m/s and observed $K = 2\pi/500$ rad/m), $m = 1.5$ and $c_\beta = 4 \times 10^{-2}$, the ratio t_r/T is 0.03. At small t_r/T, Bragg waves contrasts are $K_B \simeq |m_k|(t_r/T)(u_0/C) = 0.135 \times (u_0/C)$, where we used $m_k = -9/2$, u_0 is amplitude of IW surface orbital velocity. As reported by *Kozlov et al.* [2014], parameter u_0/C for IWs in this area ranges around $u_0/C \propto 0.1 \ldots 0.2$, hence $K_B \approx 0.027$, which is significantly smaller than observed values in Figure 10.

What mechanism does then lead to the observed modulations of PD signal by IWs? Along with the wind forcing, short waves gain energy from mechanical disturbances of the surface by breaking waves

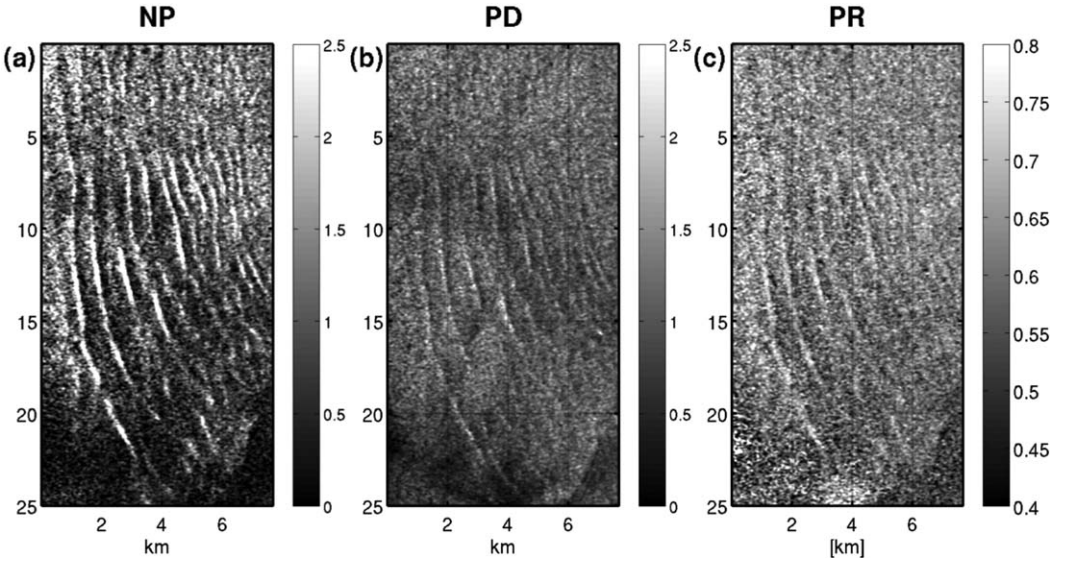

Figure 8. Enlarged fragment "1" of SAR images shown in Figure 7, depicting the surface manifestation of internal waves train: (a) NP, (b) PD, and (c) PR. Notice that NP and PD values are scaled by the corresponding mean values.

[*Kudryavtsev and Johannessen*, 2004]. Depending on wavenumber, relaxation-scale range of breaking waves is wide enough to be modulated by IWs. Thus enhanced roughness patches produced by wave breaking are responsible for the IW manifestation in both NP and Bragg scattering.

4.2. Coastal Currents

Next we consider the RADARSAT scene shown earlier in Figure 4. The main common feature of VV, PD, NP, and CP images in Figure 12 is a dark area adjacent to the coast, which coincides with a cold SST front (see Figure 1). As known and often reported [see, e.g., *Beal et al*., 1997; *Kudryavtsev et al*., 2005, and references therein], the spatial variations of the SST alter stratification of the marine atmospheric boundary layer (MABL) and subsequently the surface wind stress. Suppression of wind stress over cold sector of the front results in suppression of both short wind waves and wave breaking. This suppression is well visible in the PD and NP images, as well as in the original VV and VH images. In addition, a number of wave-like patterns associated with the internal waves in the MABL are also seen in the VV, VH, PD, and NP images.

Due to weak wind dependence of the polarization ratio, the impact of the SST front and the atmospheric gravity waves are not seen in the PR image (Figure 12b). But, there is a noticeable bright line in the PR

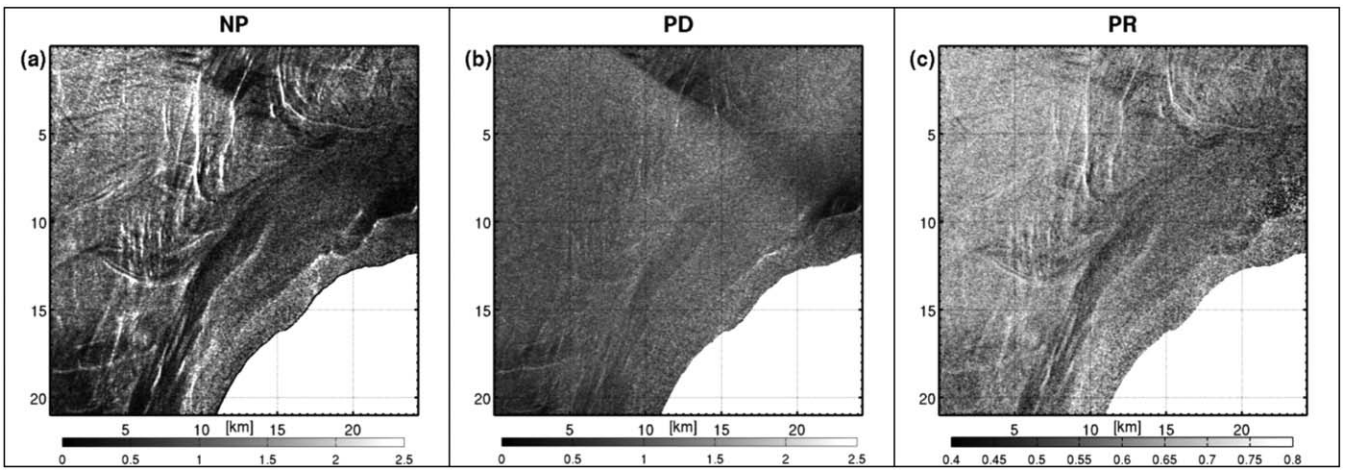

Figure 9. The same as in Figure 8, but for fragment "2" in Figure 7, depicting the "spaghetti-like" structure of IWs together with a manifestation of the coastal current.

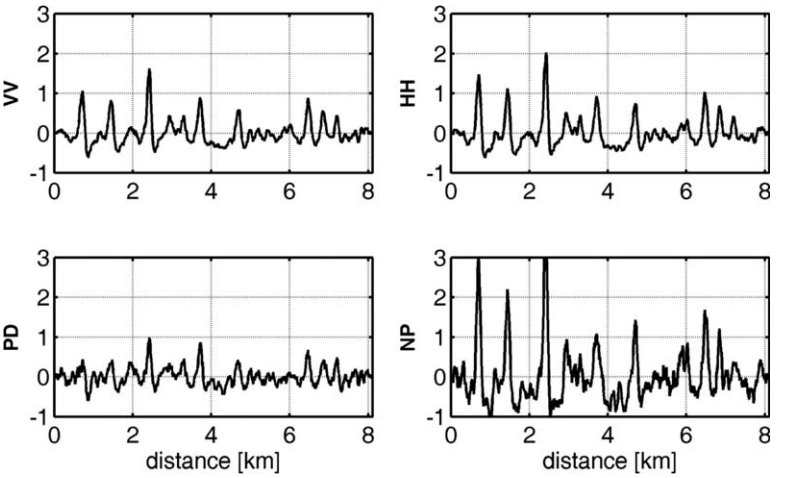

Figure 10. Profiles of the contrasts of (upper left) VV NRCS, (upper right) HH NRCS, (lower left) polarization difference, PD, and (lower right) nonpolarized contribution, NP, along the transect T1 in Figure 7 crossing a train of internal waves.

image that follows the SST frontal line. Possible origin of this bright PR feature can be interpreted as a result of the local enhancement of the NP (wave breaking) radar component (Figure 12d). The area of enhanced wave breaking traces the surface current convergence at the edge of the SST front [*Kudryavtsev et al*., 2012b].

Similarly located bright feature following the SST frontal line is also clearly manifested in the CP image (Figure 12f). Comparison of the NP and CP images reveals striking similarity between these fields, in turn suggesting that wave breaking also manifests in the cross-polarized radar signal.

High sensitivity of PD and NP signals to wind speed and relative "insensitivity" of PD signal to the surface current suggests that wind variability can be removed from NP signal in order to emphasize the remaining effect of wave breaking interactions with the surface currents. Lets decompose NP into two components, $\sigma_{wb}=\sigma^W_{wb}+\sigma^C_{wb}$, where σ^W_{wb} is the wind driven NP component, and σ^C_{wb} is the NP deviation caused by wave-current interactions. In general, the dependence of σ^W_{wb} on the polarization difference ($\Delta\sigma$) is nonlinear (Figure 5d). It also depends on the radar look direction relative to the wind direction. However, if the variability of the wind field is not too strong, the wind-driven part of NP may be linearized, $\sigma^W_{wb}-\overline{\sigma^W_{wb}}=A(\Delta\sigma-\overline{\Delta\sigma})$, where bars denote corresponding mean values and A is the regression coefficient. The part of NP anomalies caused by wave-current interactions evaluated as

$$\sigma^C_{wb}=\sigma_{wb}-\left[\overline{\sigma^W_{wb}}+A(\Delta\sigma-\overline{\Delta\sigma})\right] \qquad (9)$$

is shown in Figure 12e. Applying (9) essentially removes effects of wind variations (including wave-like patterns) from the original NP image (compare Figures 12d and 12e), thus emphasizing the bright frontal feature associated with the surface currents convergence. As such, the "refined" NP field, σ^C_{wb}, becomes very similar to the PR (see Figures 12b and 12e).

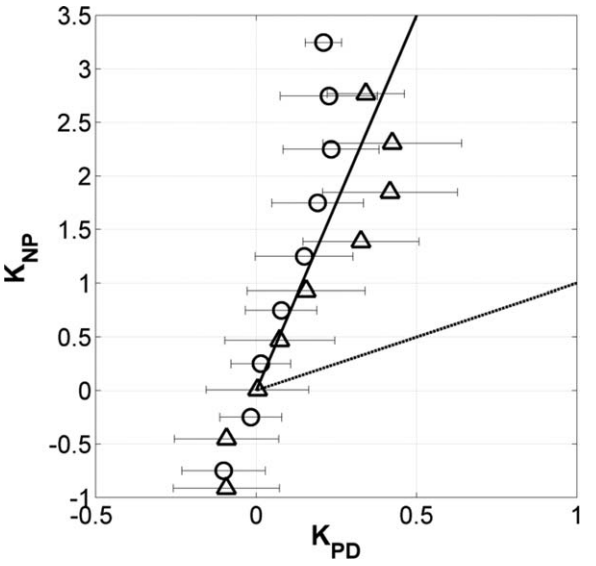

Figure 11. Scatter plot of NP contrasts versus PD contrasts. Open circles are the data for the train of IWs shown in Figure 8, and open triangles are the data for fragment with "soup" of IWs and coastal current shown in Figure 9. Horizontal lines indicate the standard deviation of the NP contrasts inside each of the NP beam. Dotted line show one-to-one relation, solid line is fit of the data: $K_{NP}=7\times K_{PD}$.

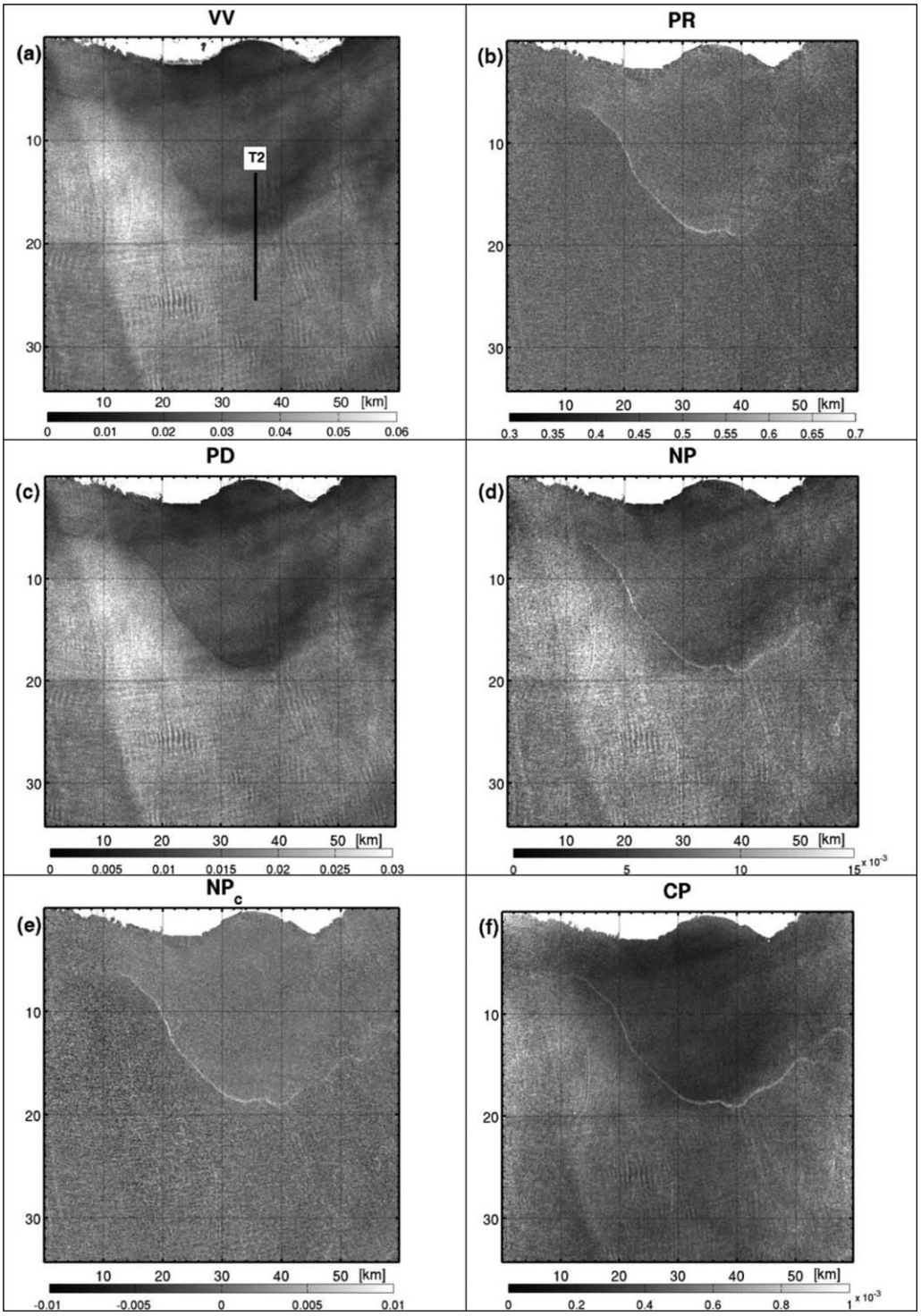

Figure 12. RADARSAT-2 quad-pol SAR data: (a) VV NRCS; (b) polarization ratio, PR; (c) polarization difference, PD; (d) nonpolarized contribution, NP; (e) NP variations caused by wave-current interaction; (f) cross-polarized, CP, NRCS. Solid line in Figure 12a shows position of transect T2 across the thermal front.

The drop in radar backscatter over the cold sector of the SST front (Figure 1) is well captured on the VV, HH, PD, and NP transects in Figure 13. Since all these quantities are dependent on the air friction velocity at the surface, this drop indicates lower u_* over the cold water due to the positive change in the atmospheric stratification.

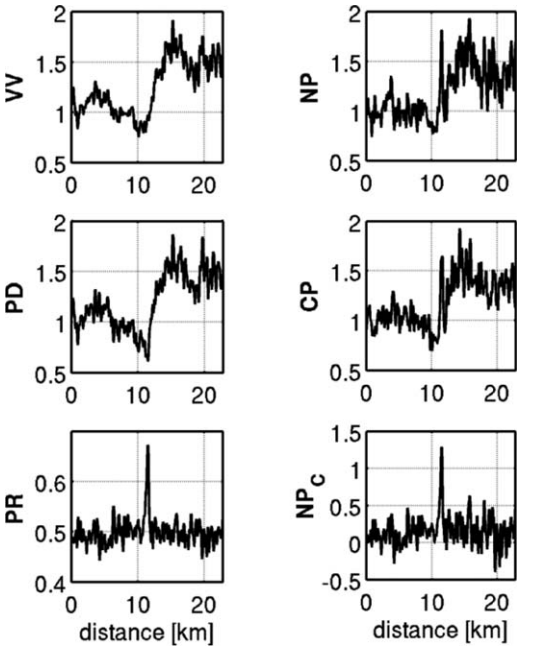

Figure 13. Transects of different components of the SAR NRCS over SST front along the line T2 shown in Figure 12a.

The observed drop in the VV NRCS can be compared with an empirical relation suggested by *Kozlov et al*. [2012]:

$$\Delta\sigma^{VV}[dB]=a|\mu_f|^4/\left(1+b|\mu_f|^4\right), \qquad (10)$$

where $a=-8.1\times10^{-6}$ and $b=10^{-6}$ are empirical constants, $\mu_f=\kappa^2(g/T_K)\cdot\Delta\theta_s/fU_{10}$ is the stratification parameter of the SST front, $\Delta\theta_s$ is the SST drop across the front, U_{10} is the wind speed on the warm side of the front, f is the Coriolis parameter, $\kappa=0.41$ and g/T_K are the von Karman constant and the atmospheric buoyancy parameter, T_K is the air temperature in °K. equation (10) predicts σ^{VV} change between -2.5 and -1.6 dB (or $\sigma^{VV}_{cold}/\sigma^{VV}_{warm}=0.55...0.69$ in linear units) at $f=1.3\times10^{-4}$, $\Delta\theta_s=4^{\circ}$C, and $U_{10}=6...7$ m/s. This estimate is in line with observed VV NRCS drop of -1.5 dB (or 0.7 in linear units; Figure 13).

Finally, we can quantitatively evaluate the relative contribution of NP part to the total backscatter signals. From (3) one may write:

$$\sigma_{wb}/\sigma^{vv}_{0B}=(P-p_B)/(1-P)$$
$$\sigma_{wb}/\sigma^{hh}_{0B}=(P/p_B-1)/(1-P). \qquad (11)$$

Using $P\approx0.5$ and $p_B\approx0.35$ (Figure 5), we find $\sigma_{wb}/\sigma^{vv}_{0B}=0.3$ and $\sigma_{wb}/\sigma^{hh}_{0B}=0.86$. These estimates suggest that background scalar radar backscattering is almost comparable to the Bragg backscattering at HH polarization. In the currents signature (see bright feature in Figure 12b), PR value increases to $P\approx0.65$ (Figure 13). For this polarization ratio the scalar backscattering is comparable to the VV Bragg backscattering and dominates over the HH Bragg backscattering, $\sigma_{wb}/\sigma^{vv}_{0B}=0.86$ and $\sigma_{wb}/\sigma^{hh}_{0B}=2.45$. This suggests that wave-current interactions result in strong relative redistribution of radar backscattering between the Bragg and wave breaking mechanisms. Assuming that Bragg waves are not changed across the front, these estimates show almost threefold enhancement of wave breaking in the convergence zone.

Both the wind variability and the wave-current interaction contribute to the CP signal. The first contribution is primarily removed in Figure 14 by considering the ratio of the cross-polarized NRCS and the polarization difference (recall that the weak wind dependence of the CP/PD was already noticed in Figure 6). The ratio CP/PD emphasizes the presence of the bright signature tracing the surface current convergence along the SST frontal line. It reflects the wave breaking enhancement at edge the SST front, the feature already noticed in the NP image (Figure 12e). Because PD is almost insensitive to the spatial surface current variations, the CP/PD ratio confirms the strong contribution of breaking and near-breaking events to the CP radar backscattering. This contribution is significant even at moderate winds of 6–7 m/s at which the RADARSAT image on 1 August 2012 was acquired. The CP/PD transect in Figure 14 shows almost a 2.5-fold increase collocated with the SST frontal position. Referring to 2.5-fold excess of the background CP/PD values over the Bragg-model (see Figure 6), one may thus translate the 2.5-fold increase of CP/PD in Figure 14 into a 3.5-fold increase of wave breaking contribution to CP, which is consistent with the observed NP enhancement in the surface current convergence zone.

5. Discussion

The present analysis confirms significant contribution of the nonresonant processes (such as breaking waves) to the sea surface C-band radar backscattering at moderate winds. This conclusion is supported by the original quad-polarization SAR data and their derived decomposition quantities. In particular, this is evidenced by the strong deviations of the PR (see Figure 5a) and the CP/PD ratio (see Figure 6c) from the two-

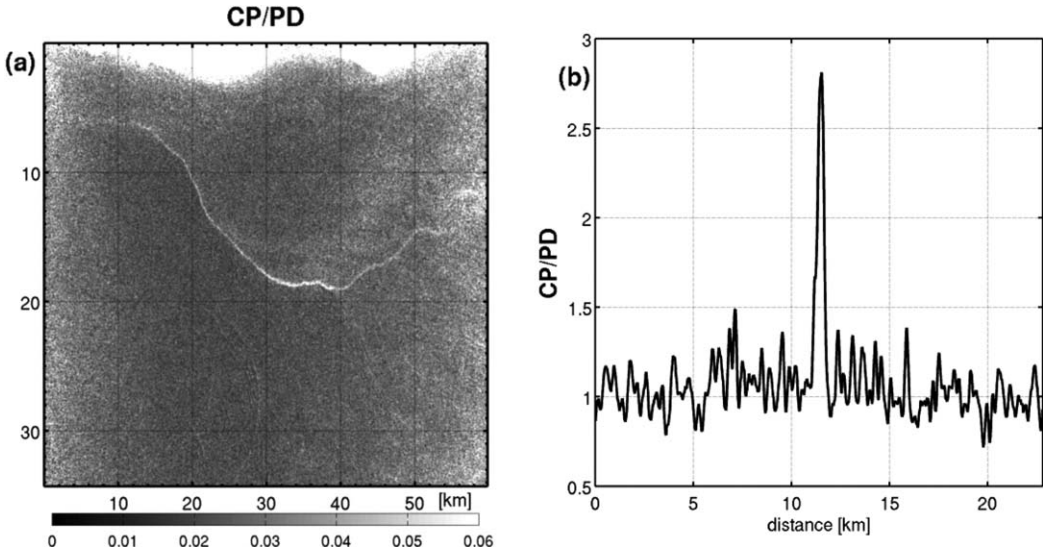

Figure 14. (a) Ratio of cross-polarization NRCS to the polarization difference, CP/PD. (b) Transect of the ratio CP/PD over the SST front along the line T2 shown in Figure 12a.

scale Bragg model. The present analysis clearly demonstrates strong and coherent response of the NP and the CP signals to the local wave-current interactions. In contrast, the impact of wave-current interactions on the modulation of the PD signal (reflecting the Bragg waves) is much weaker. While the wave breaking contribution is nonnegligible for the background conditions (away from the spatially varying surface currents) it becomes dominant for the radar signal modulation in vicinity of the current features. In the following this is further examined using the radar imaging model (RIM) of *Kudryavtsev et al*. [2005].

5.1. Impact of Breaking Waves

In accordance with RIM, the contribution of near-breaking and breaking waves to the sea surface copolarized NRCS (NP term, σ_{wb}, in equation (1)) is described by

$$\begin{aligned}\sigma_{wb} &= \int_{k<c_R k_R} \sigma_{0wb}\, dq \\ &= c_q \int_{k<c_R k_R} \sigma_{0wb} k^{-1}\, dL,\end{aligned} \tag{12}$$

where σ_{0wb} is the NRCS of an "individual" breaking zone with fractional area dq, k_R is the radar wavenumber, c_R is a constant of $O(10^{-1})$ defining the shortest breaking wave providing radar returns, dL is the length of the breaking crests in the wavenumber range from $\boldsymbol{k}$ to $\boldsymbol{k}+d\boldsymbol{k}$, and c_q is an empirical constant of order O(1). Breaking crest length is evaluated via its spectral distribution, $dL=\Lambda(\boldsymbol{k})d\boldsymbol{k}$. Since dL is also related to the energy dissipation by wave breaking, it can be estimated as [*Phillips*, 1985]:

$$dL = \alpha^{-1}\beta B dk d\varphi, \tag{13}$$

where α is the spectral constant, $\beta = c_\beta (u_*/c)^2 \cos\varphi|\cos\varphi|$ is the wind wave growth rate, c_β is growth rate parameter, and B is the saturation spectrum. Note that in the gravity equilibrium range the saturation spectrum $B \simeq \alpha\beta^{1/n_g}$ (*Kudryavtsev et al*. [2005, equation (24)]; $n_g=5$ for short gravity waves) and (13) reads:

$$dL = \beta^{(1+n_g)/n_g} dk d\varphi. \tag{14}$$

The scalar NRCS of an "individual" breaking zone, σ_{0wb}, in (12) is defined as the Physical Optics (PO) solution:

$$\sigma_{0wb} = R^2 (\sec^4\theta / s_{wb}^2) \exp\left(-\tan^2\theta / s_{wb}^2\right), \tag{15}$$

where R is the Fresnel reflection coefficient, $\theta=\theta_0+\theta'$ is the local incidence angle, θ_0 is the incidence angle of the radar observations, $\theta' = \bar{\theta}_{wb}\cos(\varphi-\varphi_R)$ is the local tilt of the breaking zone, $\bar{\theta}_{wb}$ is the mean tilt of the breaker, φ_R is the radar look direction, $s_{wb}^2=0.19$ is the mean square slope of breaking zones independent of breaking scales.

As mentioned above in the section 2 (see also Figure 5), the measured cross-polarized NRCS also significantly differs from the Bragg theory. Quasi-specular reflections from breaking wave patches also cannot contribute to cross-polarized radar backscattering [*Elfouhaily et al*., 1999; *Mouche et al*., 2007b]. The cross-polarized backscattering component appears in the second (and higher) order terms in local slope, thus leading to the CP terms depending on the local MSS and/or the local mean squared curvature [*Elfouhaily et al*., 1999; *Voronovich and Zavorotny*, 2011]. Accordingly, we assume that the cross-polarized Bragg solution (6) can be used to model the CP NRCS, either for the regular (nonbreaking) surface or the local breaking wave zones. These areas are characterized by very different "roughness" as the breaking crests roughness is much more "energetic." Suggesting isotropic breaking crest roughness, the large-scale MSS in the direction out of the radar incidence plane in (6) is half of wave breaking MSS in (15), $s_n^2=s_{wb}^2/2$. Moreover, we anticipate that the curvature spectrum of the short-scale roughness inside a breaking zone is saturated at some high level. In this case the cross-polarized (VH or HV) NRCS for an individual breaking zone is

$$\sigma_{0wb}^{vh}=c_{vh}|G_{vv}-G_{hh}|^2\frac{s_{wb}^2}{\sin^6\theta}, \tag{16}$$

where c_{vh} is an empirical constant.

Similar to (1), the wave breaking cross-polarized NRCS (16) is combined with the VH NRCS for the regular nonbreaking surface (6) as:

$$\sigma_0^{vh}=\sigma_{0br}^{vh}(1-q)+\sigma_{0wb}^{vh}q, \tag{17}$$

where $q=c_q\int k^{-1}dL$ is the fraction of the sea surface covered by breaking zones. This is consistent with conclusion reported by *Voronovich and Zavorotny* [2011] analyzing that the existence of a small fraction of the steep breaking waves can have a major contribution to the cross-polarization even at low winds. At high winds, the impact of breaking waves then fully dominates CP, as found by *Hwang et al*. [2010].

Moreover, wave breakings also serve as an additional source of resonant Bragg waves (in addition to the direct energy gain from wind). Breaking waves provide mechanical disturbances of the sea surface, and thus generate short waves [*Kudryavtsev and Johannessen*, 2004]. The rate of short wave generation by wave breaking reads [see *Kudryavtsev et al*., 2005, equation (20)]:

$$\begin{aligned}\partial E/\partial t&=\omega^3k^{-5}I_{wb}(k)\\ I_{wb}(k)&=c_b\omega^{-1}\int_0^{k_m}\omega k^{-1}dL,\end{aligned} \tag{18}$$

where $k_m=k/10$ is the upper wavenumber limit of breaking waves generating short waves at wavenumber k, and c_b is a constant.

5.2. Effect of Wave-Current Interaction

The transformation of wind waves in a nonuniform medium (varying surface currents and/or wind forcing) leads to spatial roughness variations, and thus forms radar signatures of ocean and atmospheric phenomena. Hereinafter we assume that the surface current as well as other quantities (wave spectrum modulations, etc.) may be expanded into the Fourier series

$$z(\boldsymbol{x},t)=\int\hat{z}(\boldsymbol{K})\exp\left(i(\boldsymbol{K}\boldsymbol{x}-\Omega t)\right)d\boldsymbol{K}, \tag{19}$$

where $z(\boldsymbol{x},t)$ is an arbitrary quantity, $\hat{z}(\boldsymbol{K})$ is its Fourier amplitude (complex variable), $\boldsymbol{K}$ and Ω are the wavenumber vector and the frequency. The solution of the linearized equation for the wind wave spectrum modulations by the surface current reads (see RIM for more details)

$$T(\boldsymbol{k},\boldsymbol{K})=\frac{1}{1+i\cdot r}\left[\frac{I_r}{c_g}m_k^{ij}\hat{u}_{i,j}+\frac{\tau\hat{I}_{wb}}{B_0}\right], \tag{20}$$

where $T(\boldsymbol{k},\boldsymbol{K})=\hat{B}(\boldsymbol{k},\boldsymbol{K})/B_0(\boldsymbol{k})$ is the transfer function for modulations of directional wave saturation spectrum, and r is the dimensionless relaxation parameter

$$r = l_r K(\alpha_j \beta_j - C/c_g), \tag{21}$$

where $l_r = \tau c_g/\omega$ is the relaxation scale, τ is the dimensionless relaxation time, c_g is the wave group velocity, $C = \Omega/K$ is the phase velocity of the surface currents nonuniformities, α_j and β_j are the direction cosines of the wavenumber vectors ($\boldsymbol{k}$) of the wind wave and the currents harmonics ($\boldsymbol{K}$), $m_k^{ij} = k_j \partial \ln N_0/\partial k_i$ is the tensor of the "wavenumber exponent" of the wave action spectrum N_0, $\hat{u}_{i,j}$ is the Fourier amplitude of current velocity gradient tensor $\partial u_i/\partial x_j$, term $\hat{I}_{wb}$ is the Fourier amplitude of I_{wb} (18) which describes impacts of wave breaking modulations on short-wave modulations. Note that for the sake of simplicity, the effect of varying wind forcing is not included in (20). Instead we account for wind variations through $B_0(\boldsymbol{k})$ assuming that the waves are in local balance with varying wind field.

For most of cases the relaxation scale for Bragg waves, l_r, is much smaller than the surface currents scale, $l_r K \ll 1$ (see, e.g., l_r in *Kudryavtsev et al*. [2005, Figure 6]). Therefore the direct interaction of Bragg waves with the surface currents (the straining mechanism described by the first term in equation (20)) is negligible. Thus the mechanical disturbances of the sea surface by modulated breaking waves (the second term in equation (20)) are considered as the only possible mechanism of the Bragg waves modulation by the surface currents. In this case (20) is simplified as:

$$T_s(\boldsymbol{k}_{br}, \boldsymbol{K}) = \tau \hat{I}_{wb}/B_0. \tag{22}$$

For longer waves (with wavelength of the order of a meter and longer) the spectral modulation transfer function (20) can be also represented in the truncated form, which considers the wave-current interactions as the main mechanism of modulations of these longer waves:

$$T_l(\boldsymbol{k}, \boldsymbol{K}) = (1 + i \cdot r)^{-1} (l_r/c_g) m_k^{ij} \hat{u}_{i,j}. \tag{23}$$

The length of the breaking wave crests is a nonlinear function of saturation spectrum: $dL \propto k^{-1}(B/\alpha)^{n_g+1} d\boldsymbol{k}$. The Fourier amplitude of the linear modulation of dL due to spectrum modulations then reads

$$\hat{dL}(\boldsymbol{k}, \boldsymbol{K}) = (n_g + 1) T_l(\boldsymbol{k}, \boldsymbol{K}) dL(\boldsymbol{k}), \tag{24}$$

and the Fourier amplitudes of wave breaking contributions to copolarization and cross-polarization NRCS are

$$\hat{\sigma}_{wb}^{pp}(\boldsymbol{K}) = c_q (n_g + 1) \int_{k<c_R k_R} \sigma_{0wb}^{pp} T_l(\boldsymbol{k}, \boldsymbol{K}) k^{-1} dL, \tag{25}$$

where pp is the polarization state. For $pp = vv$ and $pp = hh$ σ_{0wb}^{pp} corresponds to σ_{0wb} (15), while for the cross-polarization, $pp = vh$, σ_{0wb}^{pp} corresponds to σ_{0wb}^{vh} (16).

Combining (18), (22), and (24) gives the following Fourier amplitude of the Bragg wave modulation:

$$\hat{B}(\boldsymbol{k}, \boldsymbol{K}) = c_b (n_g + 1) \tau \omega^{-1} \int_{k<k_m} \omega T_l(\boldsymbol{k}, \boldsymbol{K}) k^{-1} dL. \tag{26}$$

The main contribution to the integrals in (25) and (26) is provided by the breaking of the equilibrium range waves. Then by using (14), (25), and (26) can be simplified as,

$$\hat{\sigma}_{wb}^{pp}(\boldsymbol{K}) = c_q \frac{n_g + 1}{n_g} \int\limits_{k<c_R k_R} d\ln k \int\limits_{-\pi/2}^{\pi/2} d\varphi \left[\sigma_{0wb}^{pp} \beta^{1/n_g} \frac{m_k^{ij} \hat{u}_{i,j}}{\omega(1 + i \cdot r)} \right], \tag{27}$$

$$\hat{B}(\boldsymbol{k}, \boldsymbol{K}) = c_b \frac{n_g + 1}{n_g} \tau \omega^{-1} \int\limits_{k<k_m} d\ln k \int\limits_{-\pi/2}^{\pi/2} d\varphi \left[\beta^{1/n_g} \frac{m_k^{ij} \hat{u}_{i,j}}{(1 + i \cdot r)} \right], \tag{28}$$

where it is taken into account that the relaxation parameter approximately reads: $\tau = (n_g \beta)^{-1}$ in the equilibrium range. Note that (28) describes the modulations of the directional spectrum. The folded spectrum, which is needed for the NRCS, is the half-sum of the directional spectrum for the two opposite directions.

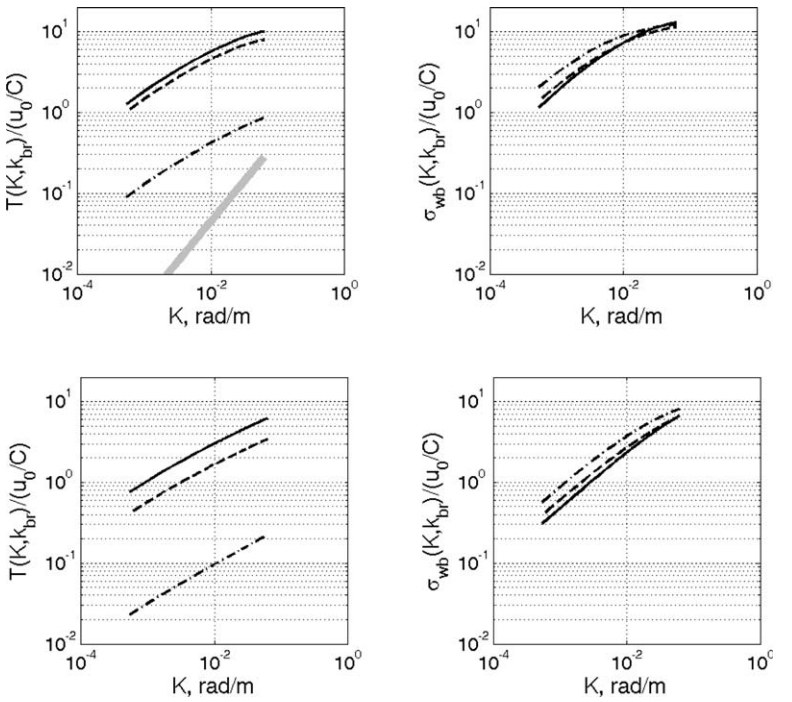

Figure 15. (left column) MTF for directional spectrum at Bragg wavenumber and (right column) MTF of wave breaking NRCS as a function of the surface current scale for wind speed 5 m/s (upper row) and 10 m/s (lower row) at the following radar look directions: up-wind (solid), cross-wind (dash), and down-wind (dash-dotted). Thick gray line in the upper left figure shows the Bragg MTF if impact of wave breaking is not included (the straining mechanism only).

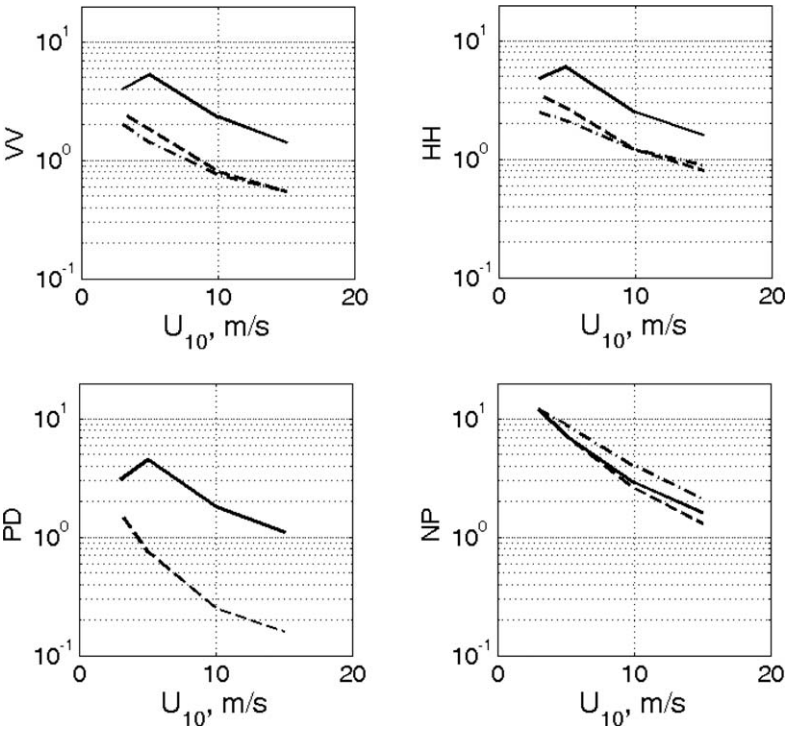

Figure 16. Amplitudes of (upper left) VV, (upper right) HH, (lower left) PD, and (lower right) NP contrasts scaled by u_0/C for IWs with $K \approx 2\pi/500$ rad/m versus wind speed for different radar look directions: cross-wind (solid lines), up-wind (dash-dotted lines), and down-wind (dashed).

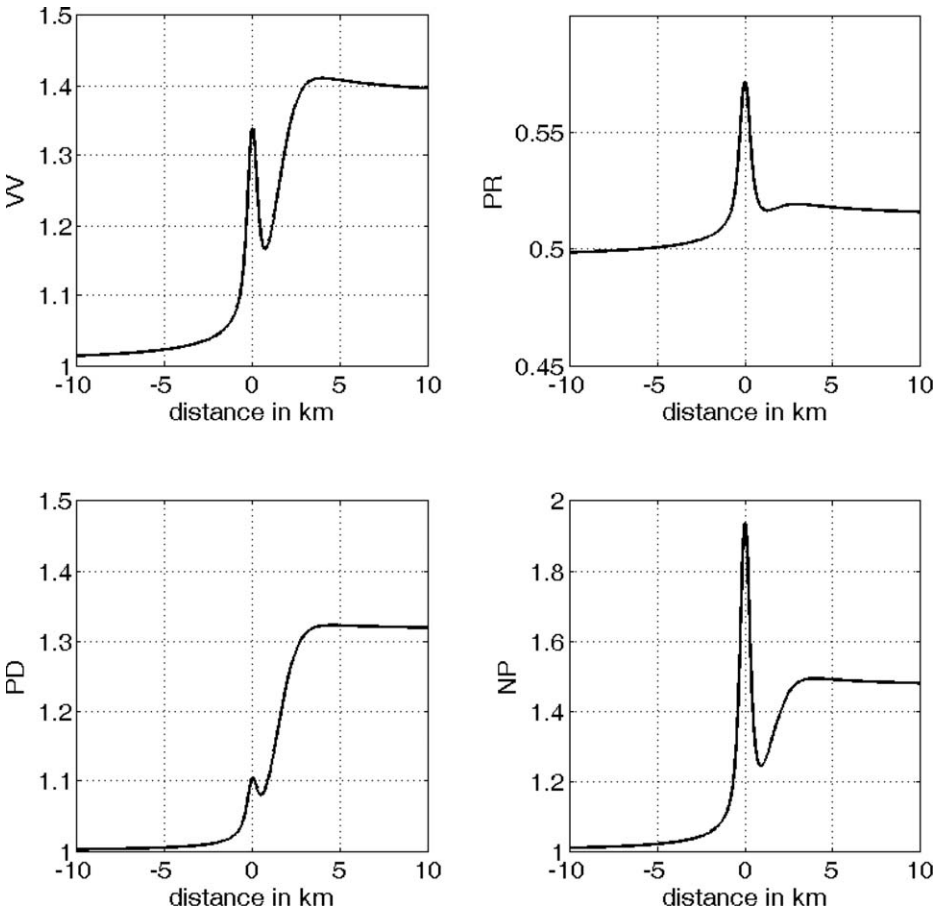

Figure 17. Model simulations of the data shown in Figure 13: (upper left) VV, (upper right) PR, (lower left) PD, (lower right) NP. The NRCS quantities are scaled by their values in the cold sector of the front.

5.3. Internal Waves

The model simulations of the radar signatures of the periodic surface current generated by the internal waves (IWs) is carried out invoking the phase velocity of the IWs of C = 0.5 m/s, and the angle between the wind velocity and the IW propagation direction of 150°.

The modulation transfer function (MTF, the Fourier amplitude of any quantity scaled by the mean value and the dimensionless surface velocity ampliude, u_0/C) for the wave spectrum at the Bragg wavenumber (28) and the wave breaking NRCS (27) are shown in Figure 15. Gray line in Figure 15 shows the reference MTF (no wave breaking impact) for the Bragg wave spectrum resulting from the straining mechanism only (the first term in (20)). As expected, this mechanism cannot produce any significant modulations that could be detected by SAR. The effect of wave breaking modulations (described by the second term in (20)) provides higher magnitude of MTF at the Bragg wavenumber. The MTF of the directional spectrum at the Bragg wavenumber has the highest magnitudes in the cross-wind and up-wind directions, but it is rather weak in the down-wind direction. The reason for these azimuth variations is explained by the relative contribution of the wave breaking to the Bragg spectrum. The impact of the wave breaking modulations on the Bragg wave modulations is strong at those directions where generation of short waves by breaking waves dominates. Although the magnitude of the up-wind short wave modulation is strong, its contribution to the radar backscattering MTF (folded spectrum) is weak due to the negligible spectrum level in this direction. The wave breaking NRCS MTF (Figure 15) is almost independent of the radar look direction. The MTFs in Figure 15 decrease at longer spatial scale of surface currents and higher wind speed. This behavior results from the decrease of the dimensionless relaxation scale $l_r K$ determining the magnitude of the MTF.

Referring to Figure 10 we find that observed IW-induced NP contrast is about 2. Since the NP MTF for the observed IW wavenumber $K \approx 2\pi/500$ rad/m is around 10 (see Figure 15, upper right), the observed NP

contrasts can be induced by the IWs with the dimensionless velocity $u_0/C=0.2$. This magnitude of nonlinearity is typical for the intensive IWs in this study area [*Kozlov et al*., 2014]. Multiplying simulated MTF (Figure 16) by the IWs nonlinearity of 0.2, the simulated VV, HH, and PD contrasts are about 0.75, 1.0, and 0.6, respectively, in line with observations in Figure 10.

5.4. Coastal Front

There is some uncertainty on how to model the surface currents corresponding to the cold SST front observed in Figure 1. The cold SSTs are edged by the narrow zone of enhanced breaking waves. We thus anticipate the surface currents convergence in the vicinity of the SST frontal line. Following these observations, we treat the existence of the SST front as a result of a tidal plume transporting cold water into the White Sea through the Gorlo Strait. For the simulations we specify both the SST and the surface currents as step-like functions, with a SST drop of 4°C and a current speed change of 0.7 m/s. In order to better reproduce the observations, we set the cross frontal width of the current front as 500 m, while the width of the SST front as 2 km.

The model simulations of the SAR observations discussed in the section 4.2 are shown in Figure 17. The curves show the NRCS characteristics along the transect crossing the SST front (Figure 12). These simulations were performed at a wind speed of 8 m/s directed along the front for the up-wind radar look direction, while the atmospheric boundary layer stratification is assumed neutral over the warm waters.

The common feature in Figure 17 is a step-like change of each of the quantities over the SST front predominantly caused by the change of the atmospheric stratification, resulting in a decrease of the wind stress and hence the surface roughness in the cold sector of the front. This feature is less pronounced in the PR, which weakly depend on wind speed. The surface current convergence strongly intensifies wave breaking, thus leading to an impulse-like behavior of NP in vicinity of the SST front. The simulated behavior of the CP NRCS over the front (not shown here) is very similar to that of the NP. Simulated impact of the wave breaking enhancement on the Bragg waves in the up-wind direction is rather weak, which is consistent with observations. The strong impact of the surface currents on the NP signal (and insensitivity of polarized Bragg scattering to the currents) leads to an impulse-like behavior of the PR, in agreement with the observations in Figure 13.

6. Conclusions

This study exploits and demonstrates the potential of polarized radar measurements for studying the physics of radar imaging of upper ocean dynamics. Two SAR scenes depicting a variety of surface manifestations of internal waves, coastal current and SST front from the White Sea are examined. The SAR data and their analysis support the main idea of the radar imaging model [*Kudryavtsev et al*., 2005] by confirming the highly important role of wave breaking in controlling the surface manifestations of the upper ocean currents.

Following *Kudryavtsev et al*. [2013] we decompose the quad-polarization SAR measurements into two components. The first one relates to the polarized Bragg-type radar scattering, and the second one takes into account nonpolarized radar return associated with wave breaking.

Analysis of the background properties (averaged over SAR image) of the quad-polarization data confirmed that (i) the polarization ratio (PR, HH/VV) deviates from the two-scale Bragg scattering model and indicates significant contribution of the nonpolarized radar returns (NP) from the near-breaking and breaking waves; (ii) the ratio (CP/PD) of the cross-polarized (CP) NRCS to the polarization difference (PD) also deviates remarkably from the Bragg model, and also indicates a significant contribution of the breaking waves; (iii) the wind dependencies of the PD and the NP signals derived from the local SAR measurements exhibit expected power laws consistent with the global statistics derived from the C-band ENVISAT data by *Mouche et al*. [2012].

We found that the IW-induced NP modulations are much higher than the corresponding PD modulations evidencing that wave breaking modulation by IWs governs the radar signature. Due to the small relaxation scale of the Bragg waves, it is further argued that the observed modulations of the Bragg wave spectrum (associated with PD variations) are presumably caused by mechanical disturbances of the sea surface by modulated breaking waves.

The sea surface temperature (SST) front is well visible in all the configuration of the quad-polarization SAR signal, except for the PR. This visibility is explained by changes in winds induced by changes in atmospheric boundary layer stratification. These wind changes are not observed in the PR image because the polarization ratio is weakly wind-dependent.

SST front is edged by a narrow convergent zone. This zone becomes clearly visible as a bright line-like feature in the PR image, suggesting that its origin corresponds to enhancement of wave breaking intensity. This wave breaking enhancement is also confirmed by the NP radar signal. In contrast, the PD signal is not sensitive to the presence of the current and primarily reacts to winds.

Using the proposed methodology and set of decompositions, one can simply separate the background (wind dependent) properties from the local effects of wave-current interactions. This approach should work well in vicinity of ocean fronts, where variations of the breaking patches dominate the radar return. Once isolated, the local polarized and depolarized components can simply be analyzed.

The NP and PD data can easily be decomposed from the dual copolarized SAR measurements, thus opening a promising opportunity to discriminate surface manifestation of the ocean currents from the variable winds. The NP radar returns are supported by breaking waves which are sensitive to both the surface currents gradients and the wind variability. The latter can be removed using the coherent part of the PD. In this case the remaining part of the NP reflects the "pure" response of the wave breaking field to the presence of the surface currents.

As further demonstrated in this paper, such an analysis also unambiguously demonstrates and quantitatively evaluates the relative impact of breakers on cross-polarized signals. Indeed, the CP signal evidently correlates with the NP signal. Future availability of the Sentinel-1 SAR (to become available in the near future) providing both copolarized and cross-polarized measurements can then build on this proposed methodology to separate effects associated with surface currents and wind variability.

Future investigations could also certainly capitalize on the proposed decomposition method to advance the radar scattering models development and to exploit similar decompositions for the Doppler shift [*Chapron et al*., 2005; *Johannessen et al*., 2008]. Indeed, the contemporaneous various observations will provide different Doppler shift anomalies. Proper signal decompositions, as suggested in this paper, must then help to more consistently separate the surface current and the wave-induced impacts from the total measured polarized Doppler shifts. The surface current Doppler signals will indeed not be sensitive to polarization state, while Doppler differences are expected for the wave-induced detected motions [e.g., *Mouche et al*., 2008]. In particular, weaker and different directional sensitivity of cross-polarized signals to Doppler biases (compared to copolarized ones) are expected. Evaluation of different combinations of polarized radar signals may thus possibly help in defining new instrumental configurations (e.g., dual-beam SAR instrument to estimate surface current [*Buck et al*., 2011]), as well as to refine the framework for combining remote sensing observations to advance the help better understanding and monitoring of the upper ocean dynamics [*Kudryavtsev et al*., 2012b; *Rascle et al*., 2014].

Acknowledgments

The core support for this study was provided by the Mega-Grant of the Russian Federation Government under grant 11.G34.31.0078, to support scientific research under the supervision of leading scientists at the Russian State Hydrometeorological University. The support from RFBR (project 14-05-31454 mol_a) and the Ministry of Science and Education (assignment 5.2483.2014/K) are also acknowledged. RADARSAT is an official trademark from the Canadian Space Agency (CSA). RADARSAT-2 SAR (CSA) data were acquired within the framework of the VIGISAT project, in the framework of a FEDER grant Présage 32635, and a partnership with CLS for providing the data, under the contracts 08 GET 13M and 09 GET 11M. The Radarsat data used in this paper can be ordered via http://gs.mdacorporation.com. The authors thank Suleiman Mostamandi for providing the MM5 model wind data.

References

Alpers, W., and I. Hennings (1984), A theory of the imaging mechanism of underwater bottom topography by real and synthetic aperture radar, *J. Geophys. Res.*, *89*(C6), 10,529–10,546.

Beal, R., V. Kudryavtsev, D. Thompson, S. Grodsky, D. Tilley, V. Dulov, and H. Graber (1997), The influence of the marine atmospheric boundary layer on ERS-1 synthetic aperture radar imagery of the Gulf Stream, *J. Geophys. Res.*, *102*(C3), 5799–5814.

Buck, C., M. Aguirre, C. Donlon, D. Petrolati, and S. D'Addio (2011), Steps towards the preparation of a Wavemill mission, in *Geoscience and Remote Sensing Symposium*, pp. 3959–3962, IEEE, Vancouver, B. C., Canada, doi:10.1109/IGARSS.2011.6050098.

Chapron, B., V. Kerbaol, and D. Vandemark (1997), A note on relationships between sea-surface roughness and microwave polarimetric backscatter measurements: Results from POLRAD'96, paper presented at the POLRAD International ESA Workshop, ESTEC, Noordwijk, Netherlands.

Chapron, B., F. Collard, and F. Ardhuin (2005), Direct measurements of ocean surface velocity from space: Interpretation and validation, *J. Geophys. Res.*, *110*, C07008, doi:10.1029/2004JC002809.

Chubb, S., A. Cooper, R. Jansen, R. Fusina, and J. Lee (1999), Radar backscatter from breaking waves in Gulf Stream current convergence fronts, *IEEE Trans. Geosci. Remote Sens.*, *17*(4), 1951–1965.

Elfouhaily, T., D. R. Thompson, D. Vandemark, and B. Chapron (1999), A new bistatic model for electromagnetic scattering from perfectly conducting random surfaces, *Waves Random Media*, *9*, 33–43.

Glukhovsky, B. H. (1991), Hydrometeorology and hydrochemistry of the Seas of the USSR, in *The White Sea, Part 1: Hydrometeorological Conditions*, vol. 2, Gidrometeoizdat, Leningrad.

Guerin, C.-A., G. Soriano, and B. Chapron (2010), The weighted curvature approximation in scattering from sea surfaces, *Waves Random Media*, *20*(3), 364–384, doi:10.1080/17455030903563824.

Hwang, P. A., and W. J. Plant (2010), An analysis of the effects of swell and surface roughness spectra on microwave backscatter from the ocean, *J. Geophys. Res.*, *115*, C04014, doi:10.1029/2009JC005558.

Hwang, P. A., B. Zhang, and W. Perrie (2010), Depolarized radar return for breaking wave measurement and hurricane wind retrieval, *Geophys. Res. Lett.*, *37*, L01604, doi:10.1029/2009GL041780.

Jackson, C. R. (2007), Internal wave detection using the moderate resolution imaging spectroradiometer (MODIS), *J. Geophys. Res.*, *112*, C11012, doi:10.1029/2007JC004220.

Jakobsson, M., et al. (2012), The international bathymetric chart of the Arctic Ocean (IBCAO) version 3.0, *Geophys. Res. Lett.*, *39*, L12609, doi:10.1029/2012GL052219.
Jansen, R. W., C. Y. Shen, S. R. Chubb, A. L. Cooper, and T. E. Evans (1998), Subsurface, surface, and radar modelling of a Gulf Stream current convergence, *J. Geophys. Res.*, *103*(C9), 18,723–18,743, doi:10.1029/98JC01195.
Johannessen, J. A., V. Kudryavtsev, D. Akimov, T. Eldevik, N. Winther, and B. Chapron (2005), On radar imaging of current features: 2. Mesoscale eddy and current front detection, *J. Geophys. Res.*, *110*, C07017, doi:10.1029/2004JC002802.
Johannessen, J., B. Chapron, F. Collard, V. Kudryavtsev, A. Mouche, D. Akimov, and K.-F. Dagestad (2008), Direct ocean surface velocity measurements from space: Improved quantitative interpretation of Envisat ASAR observations, *Geophys. Res. Lett.*, *35*, L22608, doi:10.1029/2008GL035709.
Kozlov, I. E., V. N. Kudryavtsev, J. A. Johannessen, B. Chapron, I. Dailidienė, and A. G. Myasoedov (2012), ASAR imaging for coastal upwelling in the Baltic Sea, *Adv. Space Res.*, *50*, 1125–1137, doi:10.1016/j.asr.2011.08.017.
Kozlov, I., D. Romanenkov, A. Zimin, and B. Chapron (2014), SAR observing large-scale nonlinear internal waves in the White Sea, *Remote Sens. Environ.*, *147*, 99–107, doi:10.1016/j.rse.2014.02.017.
Kudryavtsev, V., and J. Johannessen (2004), On effect of wave breaking on short wind waves, *Geophys. Res. Lett.*, *31*, L20310, doi:10.1029/2004GL020619.
Kudryavtsev, V., D. Akimov, J. A. Johannessen, and B. Chapron (2005), On radar imaging of current features: 1. Model and comparison with observations, *J. Geophys. Res.*, *110*, C07016, doi:10.1029/2004JC002505.
Kudryavtsev, V., A. Myasoedov, B. Chapron, J. Johannessen, and F. Collard (2012a), Joint sun-glitter and radar imagery of surface slicks, *Remote Sens. Environ.*, *120*, 123–132, doi:10.1016/j.rse.2011.06.029.
Kudryavtsev, V., A. Myasoedov, B. Chapron, J. Johannessen, and F. Collard (2012b), Imaging meso-scale upper ocean dynamics using SAR and optical data, *J. Geophys. Res.*, *117*, C04029, doi:10.1029/2011JC007492.
Kudryavtsev, V., B. Chapron, A. Myasoedov, F. Collard, and J. Johannessen (2013), On dual co-polarized SAR measurements of the Ocean surface, *IEEE Geosci. Remote Sens. Lett.*, *10*(4), 761–765, doi:10.1109/LGRS.2012.2222341.
Liu, B., H. Yang, Z. Zhao, and X. Li (2014), Internal solitary wave propagation observed by tandem satellites, *Geophys. Res. Lett.*, *41*, 2077–2085, doi:10.1002/2014GL059281.
Lyzenga, D. R. (1996), Effects of wave breaking on SAR signatures observed near the edge of the Gulf Stream, in *Geoscience and Remote Sensing Symposium*, vol. 2, pp. 908–910, IEEE, Lincoln, Nebr., doi:10.1109/IGARSS.1996.516517.
Lyzenga, D. R., and J. R. Bennett (1988), Full-spectrum modeling of synthetic aperture radar internal wave signature, *J. Geophys. Res.*, *93*(C10), 12,345–12,354, doi:10.1029/JC093iC10p12345.
MacDonald, Dettwiler and Associates Ltd. (2013), RADARSAT-2 product format definition, *Tech. Doc. RN-RP-51–2713*, Richmond, B. C., Canada.
Marmorino, G. O., R. W. Jansen, G. R. Valenzuela, C. L. Trump, J. S. Lee, and J. A. C. Kaiser (1994), Gulf Stream surface convergence imaged by synthetic aperture radar, *J. Geophys. Res.*, *99*(C9), 18,315–18,328, doi:10.1029/94JC01643.
McWilliams, J. C., F. Colas, and M. J. Molemaker (2009), Cold filamentary intensification and oceanic surface convergence lines, *Geophys. Res. Lett.*, *36*, L18602, doi:10.1029/2009GL039402.
Mouche, A., D. Hauser, and V. Kudryavtsev (2006), Radar scattering of the ocean surface and sea-roughness properties: A combined analysis from dual-polarizations airborne radar observations and models in C-Band, *J. Geophys. Res.*, *111*, C09004, doi:10.1029/2005JC003166.
Mouche, A. A., B. Chapron, N. Reul, D. Hauser, and Y. Quilfen (2007a), Importance of the sea surface curvature to interpret the normalized radar cross section, *J. Geophys. Res.*, *112*, C10002, doi:10.1029/2006JC004010.
Mouche, A. A., B. Chapron, and N. Reul (2007b), A simplified asymptotic theory for ocean surface electromagnetic wave scattering, *Waves Random Media*, *17*(3), 321–341.
Mouche, A. A., F. Collard, B. Chapron, K.-F. Dagestad, G. Guitton, J. A. Johannessen, V. Kerbaol, and M. W. Hansen (2012), On the use of Doppler shift for sea surface wind retrieval from SAR, *IEEE Trans. Geosci. Remote Sens.*, *50*(7), 2901–2909, doi:10.1109/TGRS.2011.2174998.
Phillips, O. M. (1977), *The Dynamics of the Upper Ocean*, Cambridge Univ. Press, N. Y.
Phillips, O. M. (1984), On the response of short ocean wave components at a fixed wavenumber to ocean current variations, *J. Phys. Oceanogr.*, *14*, 1425–1433.
Phillips, O. M. (1985), Spectral and statistical properties of the equilibrium range in wind-generated gravity waves, *J. Fluid Mech.*, *156*, 505–531.
Quilfen, Y., B. Chapron, A. Bentamy, J. Gourrion, T. El Fouhaily, and D. Vandemark (1999), Global ERS 1 and 2 and NSCAT observations: Upwind/crosswind and upwind/downwind measurements, *J. Geophys. Res.*, *104*(C5), 11,459–11,469, doi:10.1029/1998JC900113.
Rascle, N., B. Chapron, A. Ponte, F. Ardhuin, and P. Klein (2014), Surface roughness imaging of currents shows divergence and strain in the wind direction, *J. Phys. Oceanogr.*, *44*, 2153–2163, doi:10.1175/JPO-D-13-0278.1.
Romeiser, R., and W. Alpers (1997), An improved composite surface model for the radar backscattering cross section of the ocean surface: 2. Model response to surface roughness variations and the radar imaging of underwater bottom topography, *J. Geophys. Res.*, *102*(C11), 25,251–25,267, doi:10.1029/97JC00191.
Shapiro, G. I., L. Latché, and A. N. Pantiulin (2003), Mixing processes in the Gorlo Strait of the White Sea, *Oceanology*, *43*(1), 26–31.
Stoffelen, A., and D. Anderson (1997), Scatterometer data interpretation: Estimation and validation of the transfer function CMOD4, *J. Geophys. Res.*, *102*(C3), 5767–5780, doi:10.1029/96JC02860.
Thompson, D. R. (1988), Calculation of radar backscatter modulations from internal waves, *J. Geophys. Res.*, *93*(C10), 12,371–12,380, doi:10.1029/JC093iC10p12371.
Valenzuela, G. R. (1978), Theories for the interactions of electromagnetic and oceanic water—A review, *Boundary Layer Meteorol.*, *13*, 61–85, doi:10.1007/BF00913863.
Vandemark, D., B. Chapron, J. Sun, G. H. Crescenti, and H. C. Graber (2004), Ocean wave slope observations using radar backscatter and laser altimeters, *J. Phys. Oceanogr.*, *34*, 2825–2842.
Voronovich, A. G., and V. U. Zavorotny (2011), Depolarization of microwave backscattering from a rough sea surface: Modeling with small-slope approximation, in *Geoscience and Remote Sensing Symposium*, pp. 2033–2036, IEEE, Vancouver, B. C., Canada, doi:10.1109/IGARSS.2011.6049530.
Voronovich, A. G., and V. U. Zavorotny (2014), Full-polarization modeling of monostatic and bistatic radar scattering from a rough sea surface, *IEEE Trans. Antennas Propag.*, *62*(3), 1363–1371, doi:10.1109/TAP.2013.2295235.
Zhang, B., W. Perrie, X. Li, and W. G. Pichel (2011), Mapping sea surface oil slicks using RADARSAT-2 quad-polarization SAR image, *Geophys. Res. Lett.*, *38*, L10602, doi:10.1029/2011GL047013.